Solidification behaviour of Pd–Rh droplets during spray atomization

N. YANG, S. E. GUTHRIE
Sandia National Laboratories, P.O. Box 969, Livermore, CA 94550, USA

S. HO, E. J. LAVERNIA
Chemical Engineering and Materials Science Department, University of California, Irvine, CA 92717, USA

Solidification microstructure in spray-atomized Pd–10 wt % Rh powders using high-pressure gas atomization was studied. The solidification cooling rate and the solidification front velocity were investigated using a transient heat-transfer finite element method. Two different atomization gases, nitrogen and helium, were considered in the modelling studies. On the basis of the results obtained, it was found that gas atomization using helium gas led to solidification cooling rates and solidification front velocities which were two times higher than those obtained using nitrogen gas. Moreover, the cooling rate and the solidification front velocity increased with decreasing powder size for both types of atomization gas. The numerically estimated solidification front velocity using finite element analysis for nitrogen gas atomization was found to be smaller than the analytically determined absolute stability velocity that is required to promote a segregation-free microstructure. This was noted to be consistent with the segregated microstructure that was experimentally observed in nitrogen gas atomized powders. In the case of helium gas atomization, however, the increased cooling rate and solidification front velocity are anticipated to promote the formation of a segregation-free microstructure in the gas-atomized powders.

1. Introduction

Over the past decades, spray atomization has evolved as the most flexible technique for the tonnage production of metal powders, because it allows for the production of a broad range of alloy compositions with extensive control over the resulting powder characteristics and properties. In most cases, spray atomization involves impinging a molten stream of metal with a high-velocity fluid which may be either gas or water, and subsequently disintegrating the molten metal stream into micrometre-sized particulates or powders. One of the factors which makes this process attractive is that the highly efficient heat convection during atomization ensures the maintenance of relatively low processing temperatures, which limit large-scale segregation and coarsening phenomena. The powders made by spray atomization are typically subject to cooling rates that fall within the rapid solidification regime [1, 2].

The solidification microstructures and associated kinetic behaviour that evolve during this rapid solidification process have been studied in numerous alloy systems [3–8]. For example, Samuel [3] studied the combined effect of alloying elements and melt superheat on the microstructure of rapidly solidified Al–Li–Co powders. His results showed that the atomized powders exhibited four types of microstructure, i.e. dendritic, cellular, equiaxed-type, and featureless structures. He also found that increasing both the cobalt content and the powder particle diameter favored transition from dendritic to cellular structure. Gupta et al. [4] provided insight into the solidification microstructures and segregation patterns that were present in Al–Ti powders. They observed that the powders with smaller sizes generally exhibited cellular microstructure and the powders with larger sizes generally exhibited dendritic microstructures. In related studies, Juarez Islas et al. [5] studied the effect of solidification front velocity on the characteristics of aluminium-rich Al–Mn alloy solutions extended by rapid solidification. They found that microsegregation-free microstructures were obtained at sufficiently high solidification rates and that the solidification front velocity required to produce this structure increased with increasing manganese level. Recently, Yang et al. [8] conducted several experiments of Pd–Rh atomization using nitrogen gas and found that the solidification rate in their experiments was not sufficiently high to prevent the rhodium depletion at interdendritic boundaries in the atomized Pd–Rh powders.

In the present study, the solidification behaviour of spray-atomized Pd–Rh droplets was investigated. The solidification cooling rate in Pd–Rh droplets that

were atomized using nitrogen gas was studied using the finite element analysis. The solidification front velocity was also estimated and compared with the analytically calculated absolute stability velocity and the solute trapping velocity. In an effort to increase the solidification cooling rate and the solidification front velocity, the same modelling was performed using helium as the atomization gas in order to explore the possibility of obtaining a segregation-free microstructure in Pd–Rh powders. Typically, helium gas offers up to an order of magnitude increase in solidification rate over nitrogen and argon gases [9, 10].

2. Experimental procedure
2.1. Processing
The experimental studies were conducted using Pd–10 wt % Rh. The phase diagram of Pd–Rh is shown in Fig. 1 [11]. The melting temperatures of palladium and rhodium are 1554 and 1963 °C, respectively. These metals have an fcc structure and are completely soluble in each other. As seen in the phase diagram, the melting temperature of Pd–10 wt % Rh is approximately 1640 °C. The physical properties of Pd–10 wt % Rh at various temperatures are listed in Table I [12]. During spray atomization, Pd–10 wt % Rh alloy was melted and superheated to 1710 °C in order to prevent premature solidification in the nozzle. The superheated Pd–Rh melt was then disintegrated into a distribution of micrometre-sized droplets using nitrogen gas with an atomization pressure of 6.89×10^3 kPa. The mass flow rate of the atomization gas and metal were 0.08 and 0.055 kg s^{-1}, respectively. To avoid oxidation of Pd–Rh alloy during processing, the experiment was conducted inside an environment chamber, which was evacuated down to 850 mtorr (1 torr = 133.322 Pa) nitrogen prior to melting and atomization. A schematic diagram of the experimental facility used in this investigation is shown in Fig. 2.

2.2. Powder size distribution
Following atomization, the solidified Pd–Rh powders were collected in a cyclone separator, and the particle size of the as-atomized powders was characterized according to the ASTM standard B214 [13]. A series of sieves were selected in order to characterize the full range of particle sizes in the powder. The size distribution of the atomized Pd–Rh powders from the experiments is shown in Fig. 3 as a logarithmic-normal relationship. Fig. 3 shows that the mass mean droplet diameter, d_{50} (50% undersize), was approximately 60 μm. Powder sizes, d_{16} and d_{84}, corresponding to the openings of the screen meshes that let through 16 and 84 wt % of the powders were 40 and 90 μm, respectively.

2.3. Microstructure
Microstructure characterization studies were conducted on the atomized powders in order to establish the morphological features and the segregation pattern of rhodium in the Pd–Rh powders. Scanning electron
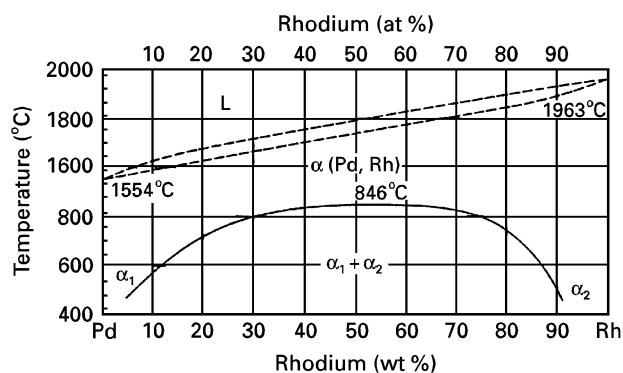

Figure 1 Phase diagram of Pd–Rh.

TABLE I Physical properties of Pd–10 wt% Rh at various temperatures [11, 12]

Temperature (K)	Thermal conductivity (W m^{-1} K^{-1})	Specific heat (J kg^{-1} K^{-1})	Density (10^3 kg m^{-3})
293	82.4	243	12.04
373	81.3	248	12.04
773	81.3	270	12.04
1273	81.3	300	12.04
1853	81.3	300	12.04
1883	33.0	375	10.52
1900	33.0	375	10.52

Liquidus temperature 1883 K
Solidus temperature 1853 K
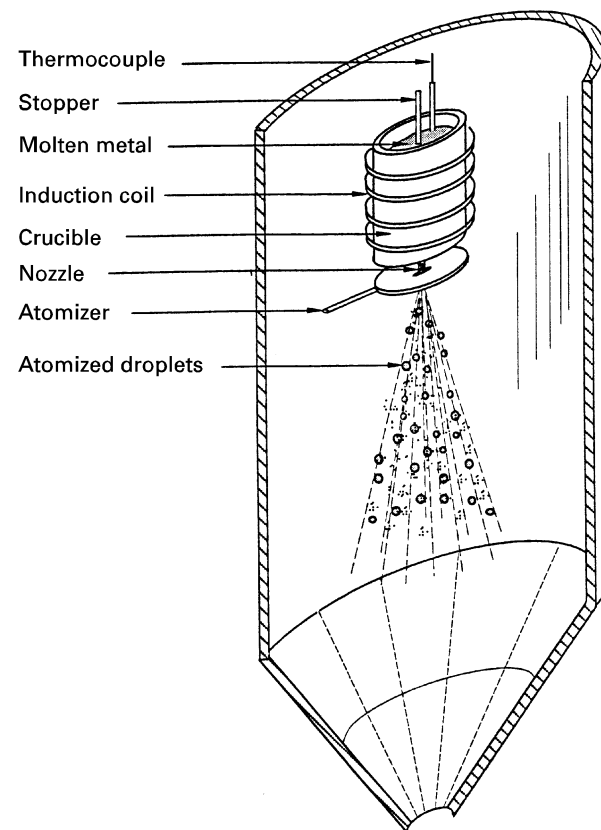Latent heat 1.632×10^5 J kg^{-1}

Figure 2 A schematic diagram of the experimental apparatus for powder production using gas atomization.

microscopy (SEM) was used to examine and analyse the microstructure of the spray-atomized powders. SEM microstructural analysis was accomplished using a Jeol 840 scanning electron microscope. For the segregation analysis, a Joel 733 electron microprobe was employed.

Fig. 4 shows a scanning electron micrograph of the spherical Pd–Rh powders. The powders consisted of fine, homogeneous, and fully spheroidal grains as shown in Fig. 5. Fig. 6 shows that the atomized Pd–Rh powders generally exhibited a typical rapid solidification microstructure consisting of a fine dendrite morphology. The micrometre-sized dendrites exhibited well-defined primary and secondary arms, and the scale of these dendrites varied as a function of powder size. The fine scale of the microstructure suggests fast solidification front velocities resulting from the highly non-equilibrium conditions that are present during atomization [14].

The concentration of palladium and rhodium in the powders as a function of distance across the powder diameter is shown in Fig. 7. Fig. 7 reveals that the concentration is relatively homogeneous and that the measured ratio of rhodium to palladium in the entire powder is very close to 0.11, which is the ratio of rhodium to palladium in the material before ato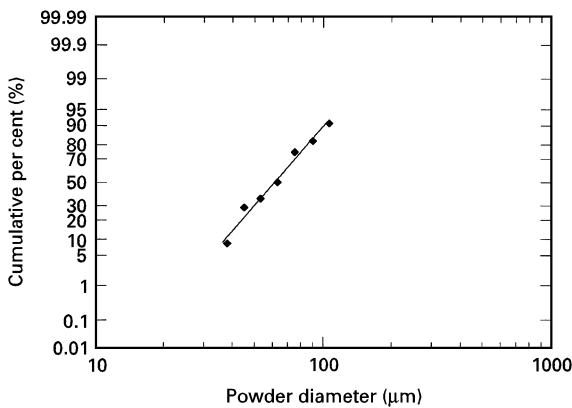mization. However, it is observed that there exists a depletion of rhodium at interdendritic boundaries, which suggests that the solidification front velocity is not sufficiently high to have segregation-free microstructure in Pd–Rh powders using nitrogen gas atomization.

3. Finite element modelling
The finite element method has been successfully used for heat-transfer problems involving phase change of materials [15–18]. In the present study, ABAQUS, a commercially available finite element code developed by Hibbitt, Karlsson and Sorenson, Inc., Pawtucket, RI, was employed in order to calculate the solidification cooling rate and the solidification front velocity in the Pd–Rh droplets.

In the finite element formulation of transient heat-transfer problems, Galerkin's method gives the following matrix equation

$$K_cT + C\dot{T} + F_h = 0 \qquad (1)$$

where T is the temperature vector, K_c is the conductivity matrix, C is the heat capacity matrix, and F_h is the

Figure 3 Powder-size distribution of gas-atomized Pd–Rh powders.

Figure 5 Scanning electron micrograph of Pd–Rh atomized powder surface.
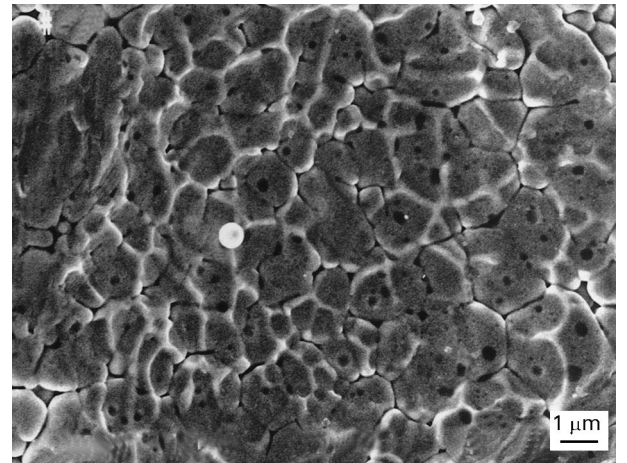

Figure 4 Scanning electron micrograph of Pd–Rh atomized powders.
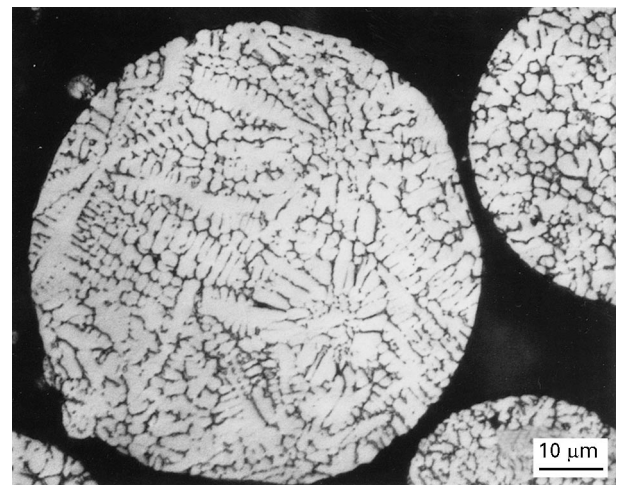

Figure 6 Fine dendrite microstructure in Pd–Rh atomized powders.

heat flow vector. The heat capacity and conductivity matrices in Equation 1 are generated using a full Gaussian integration scheme. Owing to the temperature-dependent material properties, such as thermal conductivity, density and specific heat, the matrices K_c and C in Equation 1 are temperature dependent. The matrix Equation 1, which represents a system of discrete non-linear equations, is solved using Newton's method.

In order to simulate solidification, Equation 1 must take into account the latent heat effects. The latent heat effect is approximated by a sharp increase in heat capacity with a narrow temperature range where phase change takes place. Owing to the difficulties of numerical integration in the phase-change region where the heat capacity has a sharp peak, the enthalpy, which is the integral of the heat capacity with respect to temperature, is used instead in the solution procedure [19, 20].

3.1. Geometry

Three different powder sizes, d_{16}, d_{50} and d_{84} of 40, 60, and 90 µm were modelled in the present study. Because the powder exhibits a spherical shape, three-dimensional powder may be modelled using two-dimensional axisymmetric elements. Also, due to the symmetry along the horizontal centreline, one-half of the geometry was modelled using proper symmetric boundary conditions. Initially, a coarse mesh using a relatively smaller number of elements was employed for modelling, and the number of elements was gradually increased to obtain convergent solutions. A total of 700 four-noded axisymmetric elements was used in this study. Fig. 8 shows the two-dimensional element mesh for modelling the powder with a 60 µm diameter.

3.2. Boundary and initial conditions

Initially, it was assumed that the liquid Pd–Rh droplets have a uniform temperature of 1710 °C, which corresponds to the superheat temperature. During the cooling of atomized droplets, thermal energy is transferr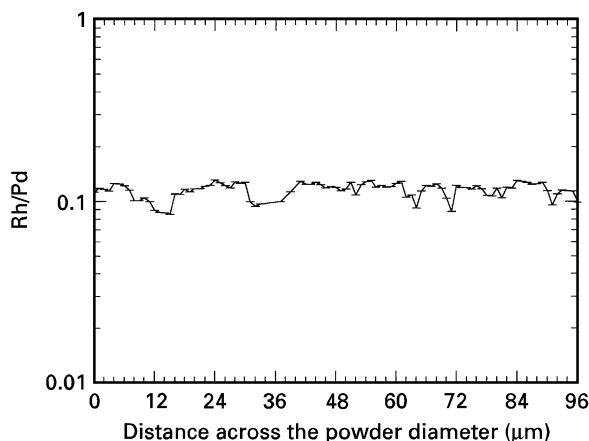ed to the atomization gas by means of thermal convection. Therefore, it is reasonable to assume that the solidification starts from the entire surface of the liquid droplet, where heat extraction takes place, and advances towards the centre of the droplet radially. The convective heat transfer coefficient, h_c, may be estimated from the Ranz–Marshall correlation [21] for the flow around spheres, which is given by

$$h_c = \frac{K_g}{d}(2 + 0.6 N_{Re}^{1/2} N_{Pr}^{1/3}) \qquad (2)$$

where K_g is the thermal conductivity of the gas, N_{Re} is the Reynolds number, and N_{Pr} is the Prandtl number. The calculated convective heat-transfer coefficients for three different powder sizes using nitrogen are listed in Table II. In an effort to increase the cooling rate, the model also uses helium as atomization gas, and its convective heat-transfer coefficients are listed in Table II as well.

4. Results and discussion

In order to obtain a segregation-free microstructure during solidification, the solidification front velocity has to exceed the velocity required for absolute stability, V_a, at which the fine dendritic growth front gives way to planar growth morphology. The velocity for absolute stability is given by [22]

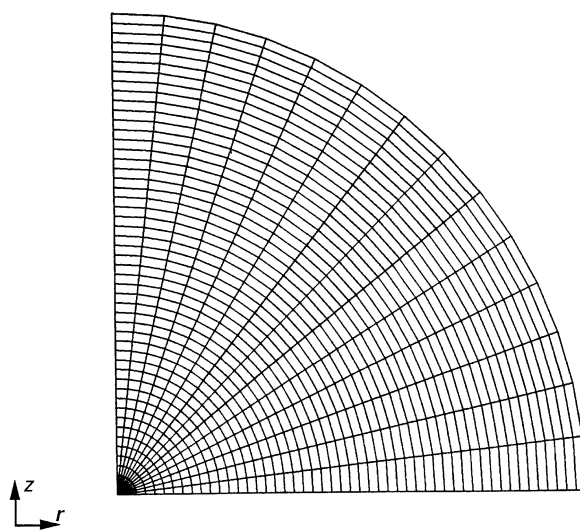$$V_a = \frac{mC_o(1 - k)D}{k^2 \Gamma} \qquad (3)$$

Figure 8 Two-dimensional axisymmetric element mesh for modelling the powder with 60 µm diameter.

TABLE II Convective heat transfer coefficients used in the analysis

Powder diameter (µm)	Convective heat-transfer coefficient (10^3 W m^{-2} K^{-1})	
	Nitrogen	Helium
40	18	42
60	15	34
90	12	27

Figure 7 Concentration of Pd–Rh in the atomized powders as a function of distance across the powder diameter.

where m is the slope of liquidus for the solidifying phase, C_o is the alloy composition, k is the solute partition coefficient (the ratio of solute concentration in solid to that in liquid) at the solid/liquid interface, D is the solute diffusion coefficient in the melt, and Γ is the Gibbs–Thomson coefficient (the ratio of solid/liquid interface surface tension to the entropy of fusion per unit volume). In Equation 3, m, k, D, and Γ are all temperature dependent, and in addition, k depends on the solidification front velocity, V, according to the relationship given by [23]

$$k = \frac{(k_o + a_o V/D)}{(1 + a_o V/D)} \quad (4)$$

where k_o is the equilibrium partition coefficient, and a_o is the interatomic jump distance from the liquid to solid at the interface. k increases with increasing solidification front velocity, and in the extreme case, increasing the solidification front velocity leads to solute trapping. The magnitude of k then approaches the limiting value of 1 (i.e. segregation-free solidification). Under these conditions, solute partitioning is completely suppressed and the critical velocity for solute trapping satisfies the equation

$$V_t = \frac{D}{a_o} \quad (5)$$

where V_t is the velocity for solute trapping at which $k = (k_o + 1)/2$. Both Equations 3 and 5 define limiting conditions for segregation-free solidification. The formation of segregation-free solid is determined by absolute stability up to some critical value of $C_o = C_o^{crit}$, at which $V_a = V_t$, given by

$$C_o^{crit} = \frac{k^2 \Gamma}{m(1 - k)a_o} \quad (6)$$

beyond which solute trapping determines the onset of formation of segregation-free solid.

Using Equations 3 and 5, the absolute stability velocity, V_a, and the solute trapping velocity, V_t, for the Pd–Rh alloy as a function of rhodium composition were calculated and shown in Fig. 9. The values of parameters employed for the calculation of V_a and V_t for the rhodium composition of 10% are listed in Table III [11, 12]. The physical properties, which were not available, were calculated. In particular, the diffusion coefficient for the liquid state of palladium was estimated using the relationship between available diffusion coefficients for the solid and the liquid states of various elements. Fig. 9 shows that V_t is significantly higher than V_a, and V_a never reaches V_t at even 100 wt % Rh. Therefore, in the Pd–Rh alloy system, V_a is the only limiting velocity for determining the velocity required for segregation-free microstructure. The calculated V_a at 10 wt % Rh was 5.21×10^{-2} m s^{-1}.

After the finite element analysis, temperatures at the surface and the centre of the Pd–Rh droplet, which has a diameter of 40 μm, as a function of cooling time are shown in Fig. 10. The temperature profile in Fig. 10 can be divided into three cooling regions. The first region is the cooling of the liquid droplet, the
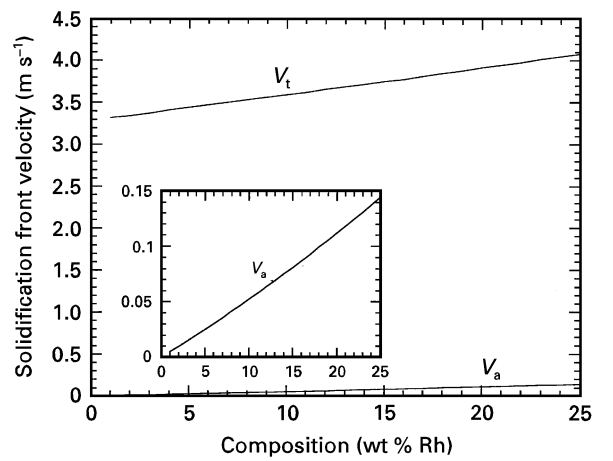
Figure 9 Calculated absolute stability velocity, V_a, and solute trapping velocity, V_t, for the Pd–Rh alloy as a function of rhodium composition.

TABLE III Parameters used for the calculation [11, 12]

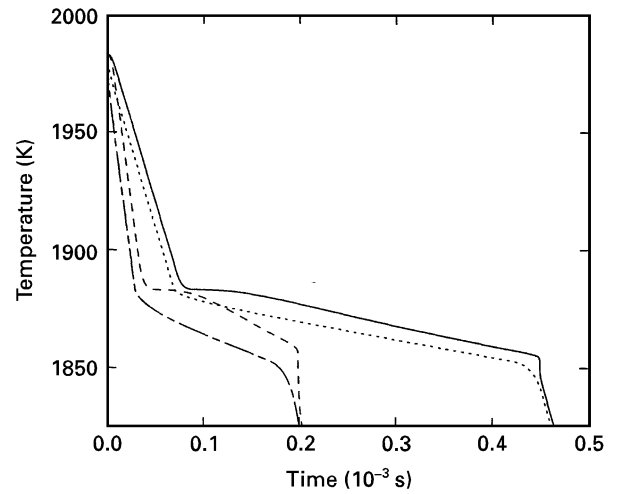| Parameter	
Atomic diameter, a_0	3.58×10^{-10} m
Liquidus slope, m	5.3 K wt %
Alloy composition, C_0	10 wt %
Partition coefficient, k	2.14
Gibbs–Thomson coefficient, G	3.2609×10^{-7} m K
Solute diffusion coefficient in the melt, D	1.2880×10^{-9} m^2 s^{-1}

Figure 10 Temperatures at (- - -, — – —) the surface and (—, - - -) the centre of a Pd–Rh droplet of size 40 μm as a function of cooling time, in (——, - - -) nitrogen and (– – –, — - —) helium.

second region is the cooling during solidification, and the third region is the cooling of the solidified droplet. Owing to the latent heat of fusion, the cooling rate during solidification is significantly reduced. When the cooling medium is helium, the cooling rate is significantly increased as compared with the case when nitrogen is used as the cooling medium. Similar trends were observed for the droplets with diameter of 60 and 90 μm. Based on Fig. 10, the solidification cooling rate and the solidification front velocity were calculated.

TABLE IV Estimated solidification cooling rate and solidification front velocities using the finite element method

	Nitrogen			Helium		
	40 μm	60 μm	90 μm	40 μm	60 μm	90 μm
Solidification cooling rate (10^3 K s^{-1})	87.1	38.0	16.9	27.1	96.3	42.6
Solidification front velocity (10^{-2} m s^{-1})	5.27	3.52	2.34	11.8	7.85	5.23

Table IV lists the calculated solidification cooling rate and solidification front velocity for three different powder sizes. It was observed that both solidification cooling rate and front velocity increase with decreasing powder size. Helium gas atomization resulted in a cooling rate and a solidification front velocity increase of approximately 2.5 and 2.2 times, respectively, as compared with those obtained using nitrogen gas atomization.

As compared with the calculated V_a, the numerically estimated solidification front velocity using nitrogen gas atomization generally exhibits smaller values. This implies that a segregated microstructure will evolve in the powders during solidification, consistent with the experimentally performed segregation analyses. Even though more than a two-fold increase is expected in the solidification front velocity when helium is used as atomization gas, it is somewhat uncertain to predict that the increased velocity is sufficiently high enough to promote the formation of a segregation-free microstructure in the powders. This is due to the fact that the analytically calculated values of V_a using Equation 3 are strongly dependent on the solute diffusion coefficient, D, in the melt, which is not available in the literature. This is the topic of current research.

5. Conclusions

1. A segregated microstructure was observed in the nitrogen gas-atomized Pd–Rh powders. The depletion of rhodium at interdendritic boundaries suggested that the solidification front velocity during atomization is not sufficiently high.

2. Numerically estimated solidification front velocities using finite element analysis for nitrogen gas atomization were found to be smaller than the analytically calculated absolute stability velocity values that are required to promote the formation of a segregation-free microstructure.

3. In the Pd-Rh alloy system, the absolute stability velocity is the only limiting factor governing the formation of a segregation-free microstrucutre.

4. When helium gas was employed in the calculations, the solidification cooling rate and the solidification front velocity were increased two-fold as compared with those when nitrogen gas was used.

5. The calculated solidification cooling rate and the solidification front velocity both increase with decreasing powder size for both nitrogen and helium gases.

6. Even though helium gas atomization gives higher solidification front velocity, it is somewhat difficult to predict that the increased velocity is sufficiently high enough to promote the formation of a segregation-free microstructure. This is due to uncertainties in available diffusion data.

References
1. H. JONES "Rapid Solidification of Metals and Alloys" Monograph 8 (The Institution of Metallurgists, London, 1982).
2. M. COHEN, B. H. KEAR and R. MEHRABIAN, in "Rapid Solidification Processing: Principles and Technology II", edited by R. Mehrabian, B.H. Kear and M. Cohen (Claitor, Baton Rouge, LA, 1980) p. 1.
3. F. H. SAMUEL, *Metall. Trans.* **17A** (1986) 73.
4. M. GUPTA, F. A. MOHAMED and E. J. LAVERNIA, *Scripta Metall.* **26** (1992) 697.
5. J. A. JUAREZ ISLAS, H. JONES and W. KURZ, *Mater. Sci. Engng* **98** (1988) 201.
6. X. ZENG, E. J. LAVERNIA and J. M. SCHOENUNG, *Scripta Metall.* **8** (1995) 1203.
7. E. J. LAVERNIA, *Int. J. Rapid. Solidif.* **5** (1989) 47.
8. N. YANG, S. E. GUTHRIE, S. HO and E. J. LAVERNIA, *J. Mater. Synth. Process.* (1995) submitted.
9. A. LAWLEY, *Int. J. Powder Metall. Powder Technol.* **13** (1977) 169.
10. H. KOHA and A. LAWLEY, "Powder Metallurgy Processing: New Techniques and Analysis" (Academic Press, New York, 1978).
11. "Metals Handbook: Metallography, Structures, and Phase Diagrams" (American Society for Metals, Metals Park, OH, 1987) p. 330.
12. E. A. BRANDES and G. B. BROOK (eds), "Smithells Metals Reference Book", 7th Edn (Butterworth-Heinemann, Jordan Hill, Oxford, 1992) pp. 13–118.
13. "Metals Handbook: ASTM B214 in Powder Metallurgy" (American Society for Metals, Metals Park, OH, 1984) p. 214.
14. R. MEHRABIAN, *Int. Metall. Rev,* **24** (1982) 185.
15. S. G. R. BROWN and J. A. SPITTLE, *Mater. Sci. Technol.* **6** (1990) 543
16. R. W. LEWIS and P. M. ROBERTS, *Appl. Sci. Res.* **44** (1987) 61.
17. K. HO and R. D. PEHLKE, *Mater. Sci. Technol.* **3** (1987) 466.
18. S. HO and A. SAIGAL, *Scripta Metall.* **31** (1994) 351.
19. "ABAQUS Users' Manual" (Hibbitt, Karlsson, and Sorensen, Inc., Pawtucket, RI, 1994).
20. "ABAQUS Theory Manual" (Hibbitt, Karlsson, and Sorensen, Inc., Pawtucket, RI, 1994).
21. J. SZEKELY, J. W. EVANS and H. Y. SOHN, "Gas-Solid Reactions" (Academic Press, New York, 1976).
22. H. JONES, *Philos. Mag.* **61** (1990) 487.
23. M. J. AZIZ, *Mater. Sci. Engng* **98** (1988) 339.